



Nickel polyphthalocyanine with electronic localization at the nickel site for enhanced CO₂ reduction reaction

Kejun Chen^a, Maoqi Cao^{a,b}, Ganghai Ni^a, Shanyong Chen^a, Hanxiao Liao^a, Li Zhu^{a,d}, Hongmei Li^a, Junwei Fu^a, Junhua Hu^c, Emiliano Cortés^{d,*}, Min Liu^{a,*}

^a State Key Laboratory of Powder Metallurgy, School of Physical and Electronics, Central South University, Changsha 410083, China

^b School of Chemistry and Chemical Engineering, Qiannan Normal University for Nationalities, Duyun 558000, China

^c School of Materials Science and Engineering, Zhengzhou University, Zhengzhou 450002, China

^d Nanoinstitut München, Fakultät für Physik, Ludwig-Maximilians-Universität München, 80539 München, Germany

ARTICLE INFO

Keywords:

Nickel polyphthalocyanine
Electrocatalysis
Electronic localization
Ni–N₄ site
CO₂ reduction reaction

ABSTRACT

Nickel phthalocyanine (NiPc) can be at first glance a compelling catalyst for CO₂ reduction reaction (CO₂RR) because of its Ni–N₄ site. Unfortunately, the pristine NiPc possesses a low catalytic activity resulting from the poor CO₂ adsorption and activation capabilities of the electron-deficiency Ni site. Herein, we develop nickel polyphthalocyanine (NiPPc) with extended conjugation to tailor the electronic density at the Ni active site. The enlarged π conjugation of NiPPc evokes the d-electrons localization, increasing the electronic density at the Ni site, which enhances its CO₂ adsorption and activation. Consequently, NiPPc supported on carbon nanotubes (NiPPc/CNT) in a flow cell delivers an excellent activity of -300 mA cm^{-2} for CO₂RR with the CO selectivity of 99.8%, which is much higher than that of NiPc dispersed on carbon nanotubes. NiPPc/CNT exhibits an outstanding stability for CO₂RR of more than 30 h at a current density of -100 mA cm^{-2} with an ultrahigh selectivity for CO, exceeding 99.7%. This work showcases a new way of tuning the electronic density of catalytic sites.

1. Introduction

Electrocatalytic reduction of CO₂ to chemicals by the electricity from clean and renewable energy sources appears as a promising route to achieve the goal of “carbon-neutral” economy [1–4]. To facilitate transformation of CO₂ into value-added chemicals, single-site transition metals possess a coordination-unsaturated site for CO₂ adsorption and activation [5–8], and thus have emerged as competitive electrocatalysts to conquer the inert CO₂ molecule for CO₂ reduction reaction (CO₂RR) [9–13]. Among these single-site catalysts, nickel phthalocyanine (NiPc) with an outstanding selectivity is particularly compelling because of its special Ni active site and reaction energy barrier for CO₂RR [14–18]. However, the original NiPc suffers from inferior activity caused by the poor CO₂ adsorption and activation from the electron-deficiency Ni site [2,19,20]. Therefore, tuning the electronic density of Ni site is crucial for promoting CO₂RR of NiPc system.

As for NiPc, there is a strong correlation between the localized d electrons of Ni atom and delocalized π electrons of the phthalocyanine ligand [21–23]. Thus, the electron density of Ni site in NiPc can be

modulated by the π system of macrocyclic ligand [24,25]. The polymerized phthalocyanines possess the extended conjugation system of the aromatic framework [26,27]. Moreover, extending π conjugation of metal macrocycle enables a much enhanced delocalization of π electrons in conjugation system [28], which can reduce the negative charges of ring ligand [29]. Conversely, the electrons of metal center can be more localized than counterpart of the pristine metal macrocycle, which can increase the electronic density of metal site. Stimulated by those situations, the polymerized NiPc with enlarged conjugation is expected to adjust the electronic structure of Ni atom and to improve the activity of NiPc for CO₂RR.

Herein, we establish nickel polyphthalocyanine (NiPPc) supported on carbon nanotubes (NiPPc/CNT) for efficient CO₂RR. NiPPc with the extended π conjugation enhances the delocalization of π electrons and promotes the d electrons Ni site to localize, leading to an enhanced electronic density of Ni site than that of NiPc. The increased electronic density of Ni site in NiPPc/CNT shows a much enhanced CO₂ adsorption and activation. As a result, NiPPc/CNT delivers a higher activity and stability for CO₂RR comparison to counterparts of NiPc supported on

* Corresponding authors.

E-mail addresses: Emiliano.Cortes@lmu.de (E. Cortés), minliu@csu.edu.cn (M. Liu).

<https://doi.org/10.1016/j.apcatb.2022.121093>

Received 3 December 2021; Received in revised form 29 December 2021; Accepted 9 January 2022

Available online 12 January 2022

0926-3373/© 2022 The Author(s). Published by Elsevier B.V. This is an open access article under the CC BY license (<http://creativecommons.org/licenses/by/4.0/>).

carbon nanotubes (NiPc/CNT). Furthermore, employing NiPPc/CNT to catalyze CO₂ reduction can maintain stable performance at the current density of -100 mA cm^{-2} for 30 h with an ultrahigh selectivity of exceeding 99.7%, indicating the outstanding stability of NiPPc/CNT for CO₂RR. This work provides a new approach to adjust electronic structure of NiPc and discloses the effect of electronic density of Ni site on CO₂RR performance.

2. Experimental section

2.1. Chemicals

Commercial NiPc, dimethylformamide (DMF), potassium bicarbonate (KHCO₃, AR), phthalocyanine (H₂Pc), nickel acetate tetrahydrate (Ni(CH₃COO)₂•4H₂O) and 1,2,4,5-tetracyanobenzene were bought from Shanghai Aladdin reagent co. Ltd. All of those chemical reagents were used as received without any other purification. Carbon nanotube (Tanfeng Tech. Inc.) was treated with the concentrated nitric acid at 90 °C overnight to remove the impurities.

2.2. Synthesis of carbon nanotubes supported catalysts

30 mg of nickel acetate tetrahydrate and 90 mg of 1,2,4,5-tetracyanobenzene were dissolved into 35 mL of absolute ethanol to form the transparent solution. And then 200 mg of the purified carbon nanotubes was added and dispersed with the aid of ultrasonic treatment. The obtained mixture was heated at 160 °C for 6 h after it transferred into a 50 mL teflon-lined stainless-steel autoclave. The as-prepared sample of carbon nanotubes supported nickel polyphthalocyanine (NiPPc/CNT) was respectively washed with the 1 M hydrogen chloride solution and hot ethanol for several times. Nickel polyphthalocyanine (NiPPc) was synthesized without adding the carbon nanotubes in a similar way. Carbon nanotubes supported nickel phthalocyanine (NiPc/CNT) was prepared by mixture of NiPc and carbon nanotubes in DMF. Briefly, NiPc (40 mg) and carbon nanotubes (100 mg) were added into 50 mL of DMF. The turbid solution underwent ultrasonical treatment for 1 h and then stirred at room temperature for 24 h. Finally, NiPc/CNT composite was collected by filtration and dried in vacuum at 60 °C for 12 h. Carbon nanotubes supported H₂Pc (H₂Pc/CNT) was prepared using H₂Pc (20 mg) with the purified carbon nanotubes (100 mg) in a similar fashion.

2.3. Materials characterizations

X-Ray diffraction (XRD) were performed on a RIGAKU Rint-2000 X-ray diffractometer equipped with graphite monochromatized Cu-K α radiation ($\lambda = 1.54184 \text{ \AA}$). Raman spectra were carried out using a Laser Micro-Raman Spectrometer (Renishaw InVia, UK). Fourier Transform Infrared Spectroscopy (FTIR) was conducted by Thermo iS50. Ultraviolet-visible spectroscopy (UV-Vis) was measured using Shimadzu UV-2600. Inductively coupled plasma optical emission spectrometry (ICP-OES) was performed on PerkinElmer Optima 8300. X-ray photoelectron spectroscopy (XPS) was implemented by Thermo ESCALAB 250XI. Scanning electron microscope (SEM) was measured by TESCAN MAIA3. Transmission electron microscope (TEM) is obtained by Titan G2 60-300 with image corrector. The CO₂ adsorption and Brunauer-Emmett-Teller specific surface areas of samples were measured using Micromeritics ASAP 2020. The thermogravimetric experiments were carried out on TG 209 F3 Tarsus from the room temperature to 900 °C with a heating rate of 10 °C min⁻¹ in the atmosphere of high-purity argon (Ar). The CO₂ temperature programmed desorption (CO₂-TPD) of the samples was measured using a BIAODE PCA-1200 apparatus equipped with a thermal conductivity detector. 100 mg of carbon nanotubes supported catalysts were pretreated at 250 °C and purged with high-purity Ar for 1 h, and cooled down to the room temperature. And then, the pretreated catalyst was purged high-purity CO₂ (99.999%) for 10 h. Moreover, CO₂ adsorption-saturated catalyst was further

purged with the high-purity Ar for 1 h. Finally, the CO₂-desorption signal was recorded under the atmosphere of high-purity Ar. ¹HNMR spectrum were measured by using a Bruker AVANCE III 400 M spectrometer.

2.4. Electrochemical measurements

Electrochemical measurements were conducted on Auto Lab at room temperature. The flow cell performances were measured using a home-made cell including sandwich of gaskets, flow frames and an anion-exchange membrane (Selemion DSVN). The window for electrolysis of CO₂ is set at $0.5 \times 2 \text{ cm}^2$. 6 mg of prepared catalysts were separately dispersed into 2 mL of ethanol with 100 μL of Nafion (5 wt%) and 400 μL of H₂O, forming a homogenous suspension. A $1 \times 3 \text{ cm}^2$ gas diffusion layer (GDL, SGL29BC) with the catalyst loading of 1 mg cm^{-2} were used as the working electrode, The IrO₂-coating titanium sheet was employed as the counter electrode, and an Ag/AgCl (with saturated KCl) electrode as a reference electrode. The flow rate of the electrolyte (1 M KHCO₃) was set at 10 mL min^{-1} in both of cathodic and anodic chambers. The flow rate of high-purity CO₂ (99.999%) was set at 20 sccm. The potentials in a flow cell were converted to reversible hydrogen electrode (RHE) without *iR* compensations by the equation:

$$E_{\text{RHE}} = E_{\text{Ag/AgCl}} + 0.0592 \times \text{pH} + 0.197 \quad (1)$$

The pH of 1 M KHCO₃ is 8.6. The products of CO₂RR were analyzed using an online gas chromatograph (Shimadzu, 2014C) and ¹HNMR. The gas products were analyzed by gas chromatograph. High-purity N₂ (99.999%) was employed as the carrier gas. A flame ionization detector was equipped with a nickel conversion furnace to measure a CO fraction, and a thermal conductivity detector was employed to analyze H₂ fraction. The faradaic efficiency of products was calculated according to gas chromatograph chromatogram peak based on the flowing equation:

$$FE_{\text{CO or H}_2} = x \times V \times \frac{2FP_0}{iRT} \quad (2)$$

where *x* is the fraction of products, *V* is a flow rate of CO₂, *F* is faraday constant (96485 C mol^{-1}), *P*₀ is the normal atmosphere (101, 325 Pa), *i* is the applied current, *R* is the gas constant ($8.314 \text{ J mol}^{-1} \text{ K}^{-1}$) and *T* is the room temperature (298 K). The gas products were measured by ¹HNMR.

2.5. Computation detail

All calculations were carried out by spin-polarized density functional theory (DFT) with the Vienna Ab initio Simulation Package (VASP) [30, 31]. Electron exchange correlation was expressed by the Perdew-Burke-Ernzerhof (PBE) functional within the generalized gradient approximation (GGA) [32]. To describe the ionic cores, the projector augmented wave (PAW) pseudopotential was applied [33,34]. The Monkhorst-Pack K-points were set to be $2 \times 2 \times 1$ for geometry optimization and $4 \times 4 \times 1$ for high-quality density of states (DOS) calculations. The plane wave energy cut off, and convergence criterion for electronic energy and forces were set as 500 eV, 10^{-5} eV , and 0.02 eV \AA^{-1} , respectively.

The computational hydrogen electrode (CHE) model was used to calculate the change in Gibbs free energy (ΔG) [35]. In CHE model, $\text{H}^+ + \text{e}^- \rightleftharpoons 1/2\text{H}_2(\text{g})$ was equilibrated at 0 V versus the reversible hydrogen electrode (RHE) at all pH values. According to this method, the change of Gibbs free energy (ΔG) for every elemental step is defined as:

$$\Delta G = \Delta E + \Delta \text{ZPE} - T \cdot \Delta S \quad (3)$$

The reaction energy difference between reactant and product is denoted as ΔE , $\Delta \text{E}_{\text{ZPE}}$ and $T \Delta S$ are the contributions of the zero-point energy and entropy, respectively. *T* is the temperature and set to be

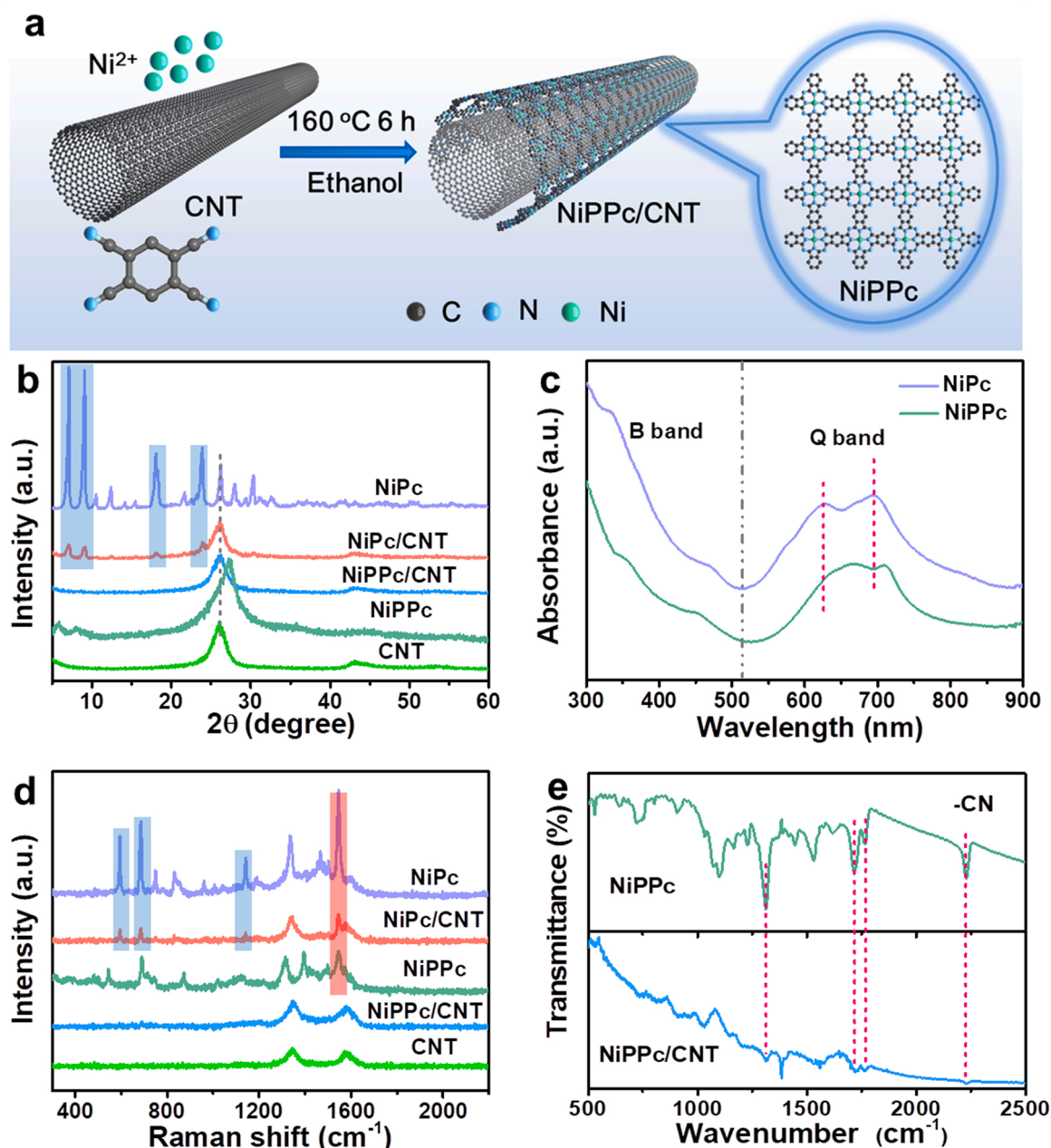


Fig. 1. (a) Schematic illustration of synthesizing NiPPc/CNT. (b) XRD patterns of samples. (c) UV-Vis spectra of NiPc and NiPPc in DMF. (d) Raman spectra of samples. (e) FTIR spectra of NiPPc and NiPPc/CNT.

298.15 K in this work.

3. Results and discussion

3.1. Synthesis and characterization of catalysts

NiPPc/CNT was synthesized by the solvothermal of 1,2,4,5-tetracyanobenzene, nickel acetate and carbon nanotubes (CNT) under 160°C for 6 h in ethanol (Fig. 1a) [36]. Compared with the NiPc, NiPPc with extended π conjugation was also prepared in a similar way without adding CNT (Fig. S1). As a control, NiPc loaded onto CNT (NiPc/CNT) was also studied. In order to detect the crystalline structure of samples, XRD characterization was conducted. The XRD pattern of NiPPc (Fig. 1b) displays three peaks at 5.8° , 8.0° and 27.4° , which are assigned to the diagonal Ni-Ni distance, neighboring Ni-Ni distance and inter-planar spacing of NiPPc, respectively (Fig. S2) [37–39].

NiPPc/CNT shows the similar XRD peaks of CNT due to the well dispersed NiPPc in NiPPc/CNT. The XRD pattern of NiPc/CNT suggests the presences of NiPc and CNT. Since phthalocyanines have unique optical properties, UV-Vis spectrum was performed to characterize samples [40]. UV-Vis spectra of NiPc and NiPPc exhibit the distinctive B-band and Q-band of phthalocyanine (Fig. 1c) [41], verifying the similar structure of NiPc and NiPPc. Noticeably, NiPPc displays a red shift in Q-band absorption in contrast to NiPc, indicating NiPPc with an extended π conjugation [42]. Those results indicate that NiPPc can be successfully synthesized and dispersed by CNT.

To investigate the structure of NiPc/CNT and NiPPc/CNT, Raman spectra were measured (Fig. 1d). Raman spectrum of NiPc/CNT displays several characteristic bands of NiPc and carbon [43,44], demonstrating the existences of NiPc and CNT in NiPc/CNT. Raman spectra of NiPc and NiPPc show an identically sensitive band at 1545 cm^{-1} , which is ascribed to the Ni interaction with phthalocyanine ring [45].

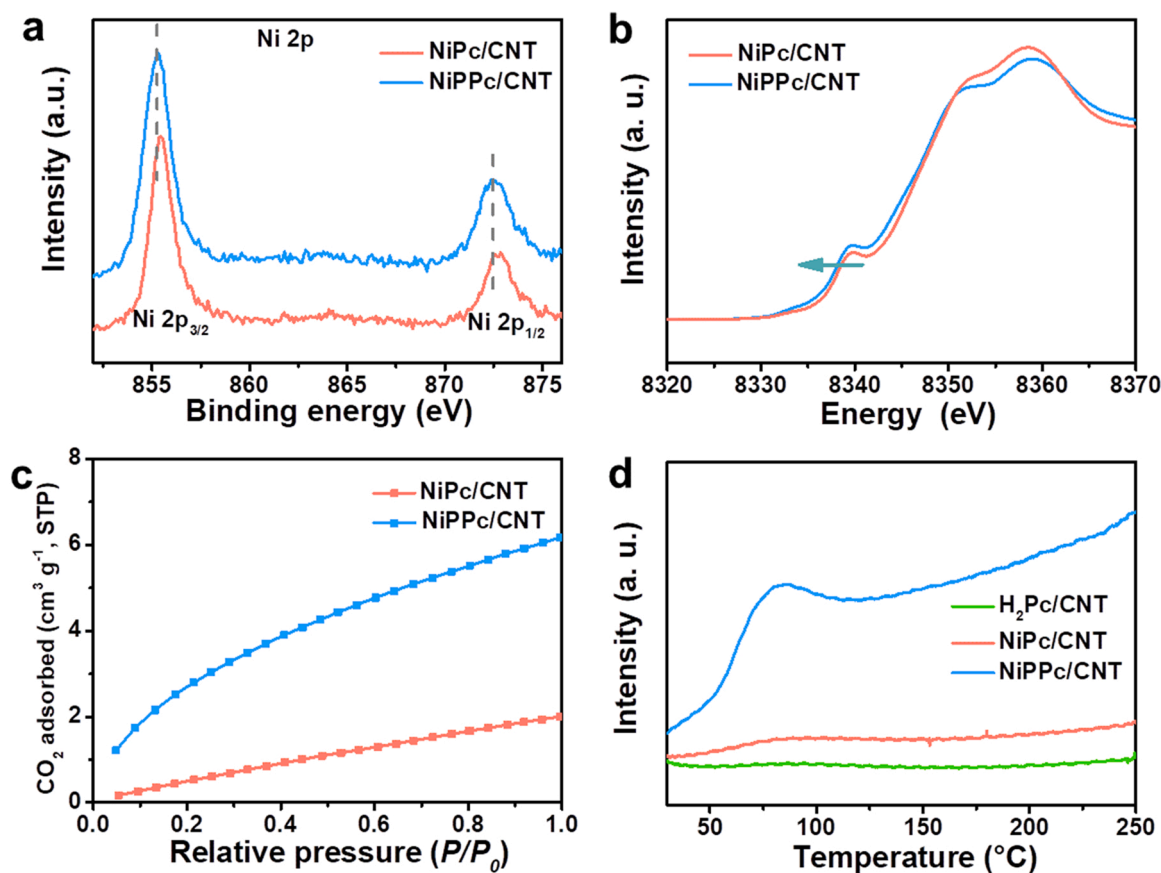


Fig. 2. (a) Ni 2p XPS spectra, (b) XANES spectra of Ni K-edge and (c) CO₂ adsorption isotherms of NiPc/CNT and NiPPc/CNT measured at 273 K. (d) TPD profiles of CO₂ desorption of H₂Pc/CNT, NiPc/CNT and NiPPc/CNT.

Additionally, the other bands of NiPPc from Raman spectrum are agreed well with the previous results [25], confirming the successful preparation of NiPPc. NiPPc/CNT shows the same absorbed bands of CNT, which can be attributed to the high dispersity of NiPPc. Moreover, FTIR spectra of NiPPc/CNT (Fig. 1e) exhibit the characteristic peaks of NiPPc, confirming the existence of NiPPc in NiPPc/CNT. Fig. S3 also demonstrates the presence of NiPc in NiPc/CNT. The absorption peak at 2230 cm⁻¹ (Fig. 1e) is assigned to stretching vibrations of the terminal cyan groups in NiPPc (Fig. S4) [46]. According to those results, NiPPc was successfully synthesized and highly dispersed on CNT to form composite catalyst of NiPPc/CNT.

The as-synthesized samples were further characterized by SEM and TEM. The pristine NiPc and NiPPc were severely aggregated to form large lumps and nanoparticles (Fig. S5), respectively. The SEM images of NiPc/CNT and NiPPc/CNT (Fig. S6) indicate the well-dispersed NiPc and NiPPc on CNT. TEM images and elemental mappings of NiPc/CNT (Fig. S7) and NiPPc/CNT (Fig. S8) display the nanowires morphology of CNT. Noticeably, some metal clusters (Fig. S7b) can be detected in NiPc/CNT due to the decomposition of NiPc to form the aggregated Ni nanoparticles under the condition of high-energy electrons. On the contrary, the NiPPc (Fig. S8b) with extended conjugation possesses high stable structure to avoid this phenomenon. Additionally, the extremely uniform distributions of N and Ni indicate that NiPPc and NiPc are well coated on CNT, respectively.

To explore the compositions and electronic structures of NiPc/CNT and NiPPc/CNT, XPS was carried out. The wide scan survey spectra (Fig. S9a) display the signals of N and Ni in NiPc/CNT and NiPPc/CNT, respectively. The Ni 2p XPS spectra were analyzed to obtain the electronic structure of Ni site. A pair of peaks of Ni 2p (Fig. 2a) in both of NiPc/CNT and NiPPc/CNT can be assigned to the Ni 2p_{1/2} and Ni 2p_{3/2} of Ni²⁺ [2,47,48]. Moreover, the NiPPc/CNT presents a negative shift at

the Ni 2p peaks in comparison to that of NiPc/CNT. To further confirm the electronic structure of Ni, X-ray absorption near-edge spectra (XANES) were performed. As displayed in XANES spectra of Ni K-edge (Fig. 2b), NiPPc/CNT shows a negative energy shift compared to counterpart of NiPc/CNT. Those results indicate that the electron can be easier localized on the Ni site of NiPPc than counterpart of NiPc. High-resolution N 1s XPS spectra (Fig. S9b) of NiPc/CNT and NiPPc/CNT display two typical peaks of N corresponding to the pyrrolic-N of Ni-N and pyridine-N [12,49]. On the basis of these results, NiPPc with extended conjugation system exhibits an increased electronic density compared to that of NiPc.

In order to understand the influence of different electronic density of the Ni site on CO₂ adsorption, the CO₂ adsorption isotherms and CO₂-TPD of NiPc/CNT and NiPPc/CNT was investigated. As shown in Fig. 2c, the CO₂ adsorption capacity of NiPPc/CNT is much higher than that of NiPc/CNT [50]. To confirm the Ni sites for CO₂ adsorption, the CO₂-TPD was measured. The phthalocyanine (H₂Pc) without the Ni site in Fig. S10 was also supported by CNT (H₂Pc/CNT) and used as control sample. The CO₂-TPD can be performed at the temperature below 250 °C due to the samples without the decomposition from thermogravimetric analysis (Fig. S11). As exhibited in Fig. 2d, NiPc/CNT shows a weak peak of CO₂ desorption before 100 °C, while NiPPc/CNT exhibits an obvious peak of CO₂ desorption. Since the H₂Pc/CNT have no signal for CO₂ desorption (Fig. 2d), the peak located before 100 °C can be assigned to the CO₂ adsorption on the Ni site. Those results indicate that NiPPc/CNT with an increased electronic density of Ni site can strengthen the CO₂ adsorption when compared with the Ni site of NiPc/CNT.

3.2. Evaluation of CO₂RR performances

Electrochemical measurements were performed to access the

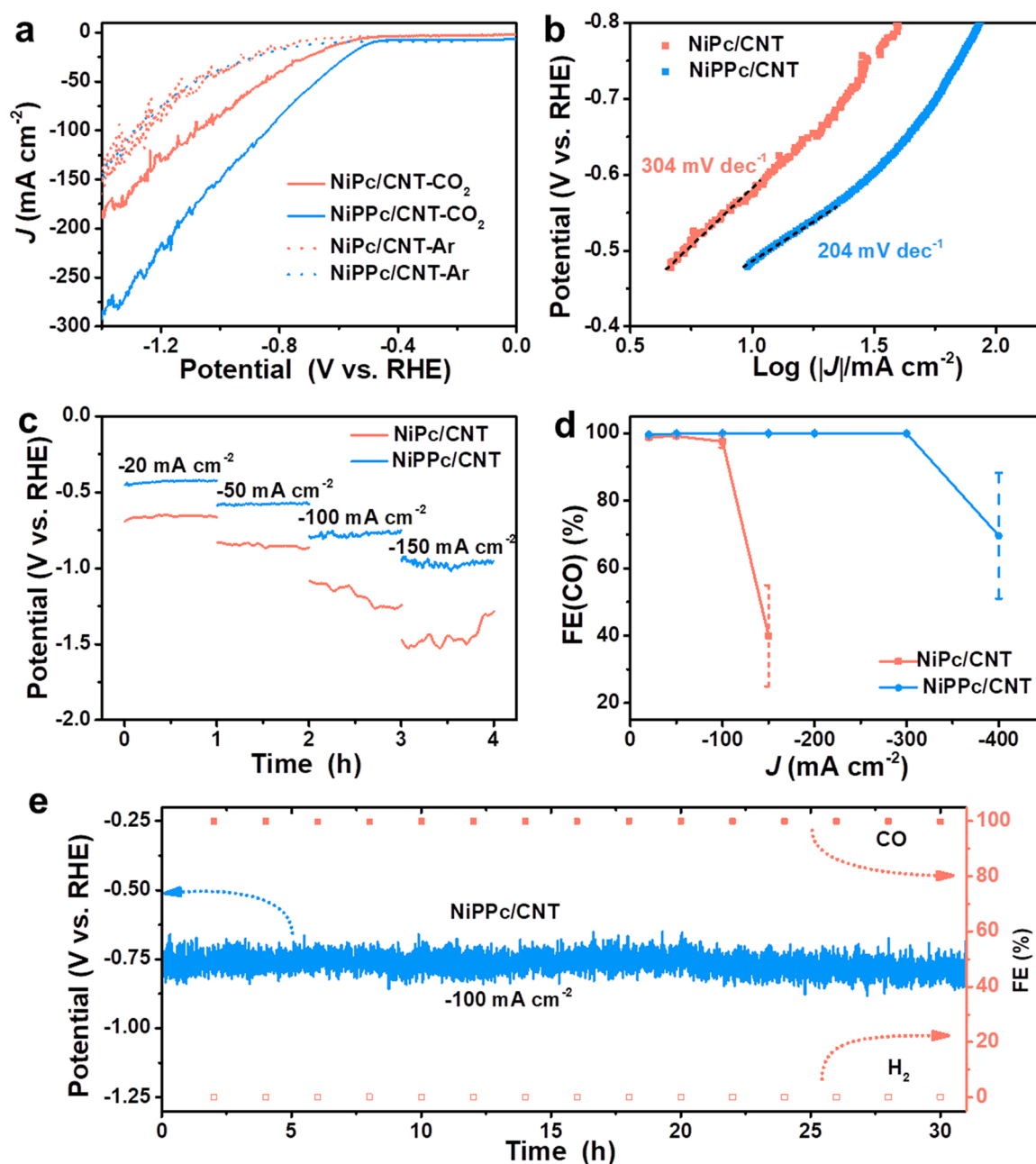


Fig. 3. (a) LSV curves of different catalysts in 1 M KHCO₃ with scan rate of 10 mV s⁻¹. (b) Tafel slopes of different catalysts. (c) Chronopotential curves of different catalysts at different current densities for CO₂RR. (d) FE(CO) of catalysts for the electrolysis of CO₂ after electrolysis for 30 min (e) The CO₂RR electrolysis at the current density of -100 mA cm⁻² for 30 h. CO₂RR performances in flow cell without *iR* correction.

catalytic performances of as-synthesized catalysts in flow cell without *iR* correction. Gas diffusion electrode (GDE) was used to transfer the gaseous CO₂ to the catalysts in flow cell (Fig. S12), which overcomes mass-transport of CO₂ in aqueous media to boost catalysts' performances for CO₂RR [51,52]. The results of inductively coupled plasma optical emission spectrometry show the approached Ni content in NiPPc/CNT (0.9282 wt%) and NiPc/CNT (0.9392 wt%). Linear sweep voltammetry (LSV) curves of catalysts in Ar and CO₂ (Fig. 3a) manifest that NiPc/CNT and NiPPc/CNT possess apparent reduction current for CO₂RR. Although NiPPc/CNT and NiPc/CNT display the same impedance of ~4 Ω (Fig. S13), NiPPc/CNT shows higher current densities for CO₂RR in comparison with NiPc/CNT (Fig. 3a), indicating a better catalytic activity of NiPPc/CNT due to its improved CO₂ adsorption of the Ni site. Accordingly, the Tafel slopes (Fig. 3b) display that NiPPc/CNT has a faster reaction dynamics than that of NiPc/CNT [53].

The CO₂RR performances of catalysts were further studied by chronopotential at various current densities (Fig. 3c). Compared with NiPc/CNT, NiPPc/CNT shows a lower overpotential to reach the same current density for CO₂RR. Moreover, NiPPc/CNT can sustain stable even at the high current density of -150 mA cm⁻², but NiPc/CNT only can keep stable at the lower current densities (less than -100 mA cm⁻² in Fig. 3c). This result indicates the polymerized NiPPc with a better activity and stability than those of the pristine NiPc.

To obtain the selectivity of products, the on-line gas chromatograph (GC) and ¹H NMR were employed to analyze the gaseous and liquid products, respectively. Only CO and H₂ can be detected by GC (Fig. S14). The ¹H NMR result (Fig. S15) presents that a very small amount of formate was produced during the electrolysis of -100 mA cm⁻² for 2 h [54]. Thus, the produced formate for CO₂RR can be neglected in this work. Fig. 3d shows the faraday efficiency of CO (FE(CO)) at different

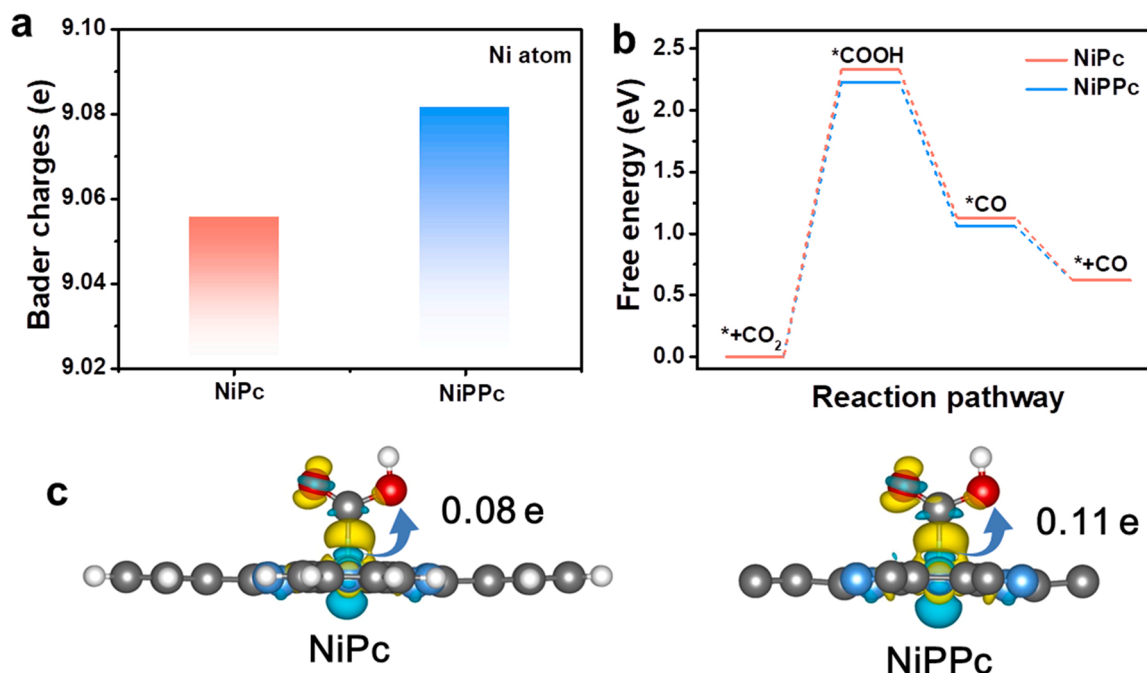


Fig. 4. (a) Bader charges of Ni atom in NiPc and NiPPc. (b) Free energy diagrams of NiPc and NiPPc for CO₂RR. (c) Different charge densities of NiPc and NiPPc when *COOH adsorbs on Ni site.

current densities. The FE(CO) of NiPc/CNT can reach to 97% up to a current density of -100 mA cm^{-2} . H₂ is a by-product of CO₂RR in this work (Fig. S16). When further increases the applied current density to -150 mA cm^{-2} , the FE(CO) is subject to a dramatic drop due to its poor CO₂ adsorption and activation. Impressively, NiPPc/CNT achieves a higher selectivity of CO (exceeding 99.8% even at -300 mA cm^{-2}), which can be attributed to the enhanced CO₂ adsorption and activation of the Ni site in NiPPc. The selectivity of NiPc-based catalysts for CO₂RR is determined by the chemical structure of molecule. This big change in the CO selectivity is rooted in the destruction of Ni–N₄ structure, as demonstrated by the previous work [10]. To confirm the origin of catalytic activity for CO₂RR, H₂Pc/CNT without active site of Ni was also studied. H₂Pc/CNT shows negligible performance for electrolysis of CO₂ to CO (Fig. S17). On the basis of those results, the Ni site in the NiPc and NiPPc is the active site for CO₂RR. Moreover, the stability of NiPPc/CNT catalyst was conducted by a consecutive electrolysis of CO₂ at a constant current density of -100 mA cm^{-2} . Fig. 3d exhibits the extremely stable selectivity (>99.7%) and potential over 30 h without any significant fluctuations, coming up to performances of the representative phthalocyanine catalysts in previous work (Table S1). The GDE of NiPPc/CNT after the long-term was also characterized. The SEM images of GDE before and after electrolysis indicate the stable morphology of NiPPc/CNT (Fig. S18). The XPS results also indicate the decent stability of catalyst during the electrolysis (Fig. S19). The high activity, selectivity and stability of NiPPc/CNT enable it as a promising catalyst for highly efficient CO₂RR.

3.3. Theoretical calculations

DFT calculations were performed to better understand the different catalysis of NiPc and NiPPc (Fig. S20). The Bader charges of Ni atom in NiPc and NiPPc were analyzed (Fig. 4a). NiPPc shows an electron-enriched Ni site compared with that of NiPc, indicating that the extended conjugation of NiPPc can induce the electronic localization on Ni site to increase its electronic density. The free energy diagrams of CO₂RR (Fig. 4b) demonstrate that the intermediates adsorbed on NiPPc is more steady than that on NiPc. The potential limiting step on Ni sites is the CO₂ activation to form *COOH. NiPPc with electronic localized Ni

site exhibits the lower ΔG_{*COOH} than counterpart of NiPc, indicating the relatively fast reaction dynamics of NiPPc [55]. The different charge densities were further analyzed to study the effects of electronic density of Ni site on CO₂ activation. As shown in Fig. 4c, the Ni site with electronic localization is conducive to transform more electrons to form *COOH in contrast to NiPc, lowering the reaction energy barrier for CO₂RR. According to those results, NiPPc with electronic localization of nickel site can facilitate CO₂ activation and thereby boost performance of CO₂RR.

4. Conclusions

In conclusion, we have proposed the polymerized NiPPc with prolonged conjugation to tailor the electronic structure of Ni site. The results of XPS and Bader charges revealed the electronic density of Ni site can be increased by the π -electrons delocalization of ligand. The results of CO₂ adsorption isotherms and CO₂-TPD demonstrated the increased electronic density was conducive to strengthen CO₂ adsorption of Ni site. NiPPc/CNT with the improved CO₂ adsorption exhibited a superior activity and an ultrahigh selectivity of CO (exceeding 99.8% at current densities went -300 mA cm^{-2} for CO₂RR), which is much better than those of NiPc/CNT in flow cell. Moreover, NiPPc/CNT delivered the outstanding stability for CO₂RR with 99.7% FE(CO) at a current density of -100 mA cm^{-2} for 30 h. Tafel slopes and DFT calculations further demonstrated that the electronic localization of Ni site can also improve the CO₂ activation. This work provided a new way to tune electronic structure and gave new insights into the electronic density of single-site catalysts for CO₂RR.

CRediT authorship contribution statement

All the authors have contributed to the design of experiments, the acquisition and analysis of the experimental data and the writing of the manuscript.

Declaration of Competing Interest

The authors declare that they have no known competing financial

interests or personal relationships that could have appeared to influence the work reported in this paper.

Acknowledgements

The authors gratefully thank the International Science and Technology Cooperation Program, China (Grant nos. 2017YFE0127800 and 2018YFE0203400), Natural Science Foundation of China, China (Grant nos. 21872174, 22002189, 22011530423 and U1932148), Hunan Provincial Science and Technology Program, China (No. 2017XK2026 and 2017TP1001), Hunan Provincial Natural Science Foundation, China (2020JJ2041, 2020JJ5691), Key R&D Program of Hunan Province, China (2020WK2002), Shenzhen Science and Technology Innovation Project, China (Grant no. JCYJ20180307151313532), Fundamental Research Funds for the Central Universities of Central South University, China (2021zzts0058). Department of Science and Technology of Guizhou Province, China ([2019]1297), Natural Science Foundation of Education Department of Guizhou Province, China ([2018]424) and Qiannan Normal University for Nationalities, China (QNY-SKYTD2018003 and QNYSKYPT2018005). We also acknowledge funding and support from the Deutsche Forschungsgemeinschaft (DFG, German Research Foundation), Germany, under Germany's Excellence Strategy – EXC 2089/1 – 390776260, the Bavarian program Solar Energies Go Hybrid (SolTech), from Bavaria, Germany; the Center for NanoScience (CeNS), from Munich, Germany; and the European Commission through the ERC Starting Grant CATALIGHT (802989), from the European Union. We are also grateful to Dr. Ying-Rui Lu and Dr. Ting-Shan Chan at TLS 01C1 and TLS 16A1 beamlines of the National Synchrotron Radiation Research Center (NSRRC) for help with characterizations.

Appendix A. Supporting information

Supplementary data associated with this article can be found in the online version at [doi:10.1016/j.apcatb.2022.121093](https://doi.org/10.1016/j.apcatb.2022.121093).

References

- J. Gu, C.-S. Hsu, L. Bai, H.M. Chen, X. Hu, Atomically dispersed Fe^{3+} sites catalyze efficient CO_2 electroreduction to CO, *Science* 364 (2019) 1091–1094.
- Y.J. Sa, H. Jung, D. Shin, H.Y. Jeong, S. Ringe, H. Kim, Y.J. Hwang, S.H. Joo, Thermal transformation of molecular Ni^{2+} -N₄ sites for enhanced CO_2 electroreduction activity, *ACS Catal.* 10 (2020) 10920–10931.
- C. Wang, H. Ren, Z. Wang, Q. Guan, Y. Liu, W. Li, A promising single-atom Co-N-C catalyst for efficient CO_2 electroreduction and high-current solar conversion of CO_2 to CO, *Appl. Catal. B* 304 (2022), 120958.
- X. Wei, S. Xiao, R. Wu, Z. Zhu, L. Zhao, Z. Li, J. Wang, J.S. Chen, Z. Wei, Activating COOH^* intermediate by $\text{Ni}/\text{Ni}_3\text{Zn}_{0.7}$ heterostructure in porous N-doped carbon nanofibers for boosting CO_2 electroreduction, *Appl. Catal. B* 302 (2022), 120861.
- F. Lv, N. Han, Y. Qiu, X. Liu, J. Luo, Y. Li, Transition metal macrocycles for heterogeneous electrochemical CO_2 reduction, *Coord. Chem. Rev.* 422 (2020), 213435.
- E. Boutin, L. Merakeb, B. Ma, B. Boudy, M. Wang, J. Bonin, E. Anxolabéhère-Mallart, M. Robert, Molecular catalysis of CO_2 reduction: recent advances and perspectives in electrochemical and light-driven processes with selected Fe, Ni and Co azo macrocyclic and polypyridine complexes, *Chem. Soc. Rev.* 49 (2020) 5772–5809.
- X. Su, K.M. McCardle, L. Chen, J.A. Panetier, J.W. Jurss, Robust and selective cobalt catalysts bearing redox-active bipyridyl-N-heterocyclic carbene frameworks for electrochemical CO_2 reduction in aqueous solutions, *ACS Catal.* 9 (2019) 7398–7408.
- Y. Lu, J. Zhang, W. Wei, D.-D. Ma, X.-T. Wu, Q.-L. Zhu, Efficient carbon dioxide electroreduction over ultrathin covalent organic framework nanolayers with isolated cobalt porphyrin units, *ACS Appl. Mater. Interfaces* 12 (2020) 37986–37992.
- M.-D. Zhang, D.-H. Si, J.-D. Yi, S.-S. Zhao, Y.-B. Huang, R. Cao, Conductive phthalocyanine-based covalent organic framework for highly efficient electroreduction of carbon dioxide, *Small* 16 (2020), 2005254.
- X. Zhang, Y. Wang, M. Gu, M. Wang, Z. Zhang, W. Pan, Z. Jiang, H. Zheng, M. Lucero, H. Wang, Molecular engineering of dispersed nickel phthalocyanines on carbon nanotubes for selective CO_2 reduction, *Nat. Energy* 5 (2020) 684–692.
- N. Corbin, J. Zeng, K. Williams, K. Manthiram, Heterogeneous molecular catalysts for electrocatalytic CO_2 reduction, *Nano Res.* 12 (2019) 2093–2125.
- D.-D. Ma, S.-G. Han, C. Cao, W. Wei, X. Li, B. Chen, X.-T. Wu, Q.-L. Zhu, Bifunctional single-molecular heterojunction enables completely selective CO_2 -to-CO conversion integrated with oxidative 3D nano-polymerization, *Energy Environ. Sci.* 14 (2021) 1544–1552.
- Y. Wu, Y. Liang, H. Wang, Heterogeneous molecular catalysts of metal phthalocyanines for electrochemical CO_2 reduction reactions, *Acc. Chem. Res.* 54 (2021) 3149–3159.
- S. Liu, H.B. Yang, S.F. Hung, J. Ding, W. Cai, L. Liu, J. Gao, X. Li, X. Ren, Z. Kuang, Elucidating the electrocatalytic CO_2 reduction reaction over a model single-atom nickel catalyst, *Angew. Chem. Int. Ed.* 59 (2020) 798–803.
- Z. Zhang, Y.-G. Wang, Molecular design of dispersed nickel phthalocyanine@nanocarbon hybrid catalyst for active and stable electroreduction of CO_2 , *J. Phys. Chem. C* 125 (2021) 13836–13849.
- N. Huang, K.H. Lee, Y. Yue, X. Xu, S. Irle, Q. Jiang, D. Jiang, A stable and conductive metallophthalocyanine framework for electrocatalytic carbon dioxide reduction in water, *Angew. Chem. Int. Ed.* 59 (2020) 16587–16593.
- D.-D. Ma, S.-G. Han, C. Cao, X. Li, X.-T. Wu, Q.-L. Zhu, Remarkable electrocatalytic CO_2 reduction with ultrahigh CO/H_2 ratio over single-molecularly immobilized pyrrolidinonyl nickel phthalocyanine, *Appl. Catal. B* 264 (2020), 118530.
- J. Su, J.-J. Zhang, J. Chen, Y. Song, L. Huang, M. Zhu, B.I. Yakobson, B.Z. Tang, R. Ye, Building a stable cationic molecule/electrode interface for highly efficient and durable CO_2 reduction at an industrially relevant current, *Energy Environ. Sci.* 14 (2021) 483–492.
- X. Yang, J. Cheng, X. Xuan, N. Liu, J. Liu, Boosting defective carbon by anchoring well-defined atomically dispersed Ni-N₄ sites for electrocatalytic CO_2 reduction, *ACS Sustain. Chem. Eng.* 8 (2020) 10536–10543.
- Z. Ma, X. Zhang, X. Han, D. Wu, H. Wang, Z. Gao, F. Xu, K. Jiang, Synergistic adsorption and activation of nickel phthalocyanine anchored onto ketjenblack for CO_2 electrochemical reduction, *Appl. Surf. Sci.* 538 (2021), 148134.
- T. Wang, W. Huang, T. Sun, W. Zhang, W. Tang, L. Yan, J. Si, H. Ma, Two-dimensional metal-polyphthalocyanine conjugated porous frameworks as promising optical limiting materials, *ACS Appl. Mater. Interfaces* 12 (2020) 46565–46570.
- Z. Honda, Y. Sakaguchi, M. Tashiro, M. Hagiwara, T. Kida, M. Sakai, T. Fukuda, N. Kamata, Phthalocyanine based metal containing porous carbon sheet, *Appl. Phys. Lett.* 110 (2017), 133101.
- Q. Zhou, Z.-F. Liu, T.J. Marks, P. Darancet, Electronic structure of metallophthalocyanines, MPC (M = Fe, Co, Ni, Cu, Zn, Mg) and fluorinated MPC, *J. Phys. Chem. A* 125 (2021) 4055–4061.
- S. Yang, Y. Yu, M. Dou, Z. Zhang, F. Wang, Edge-functionalized polyphthalocyanine networks with high oxygen reduction reaction activity, *J. Am. Chem. Soc.* 142 (2020) 17524–17530.
- S. Wei, H. Zou, W. Rong, F. Zhang, Y. Ji, L. Duan, Conjugated nickel phthalocyanine polymer selectively catalyzes CO_2 -to-CO conversion in a wide operating potential window, *Appl. Catal. B* 284 (2021), 119739.
- W.J. Youngblood, Synthesis of a new trans- A_2B_2 phthalocyanine motif as a building block for rodlike phthalocyanine polymers, *J. Org. Chem.* 71 (2006) 3345–3356.
- N. Han, Y. Wang, L. Ma, J. Wen, J. Li, H. Zheng, K. Nie, X. Wang, F. Zhao, Y. Li, J. Fan, J. Zhong, T. Wu, D.J. Miller, J. Lu, S.-T. Lee, Y. Li, Supported cobalt polyphthalocyanine for high-performance electrocatalytic CO_2 reduction, *Chem* 3 (2017) 652–664.
- J. Wen, D. Luo, L. Cheng, K. Zhao, H. Ma, Electronic structure properties of two-dimensional π -conjugated polymers, *Macromolecules* 49 (2016) 1305–1312.
- O.S. Finikova, A.V. Cheprakov, P.J. Carroll, S. Dalosto, S.A. Vinogradov, Influence of nonplanarity and extended conjugation on porphyrin basicity, *Inorg. Chem.* 41 (2002) 6944–6946.
- G. Kresse, J. Furthmüller, Efficiency of ab-initio total energy calculations for metals and semiconductors using a plane-wave basis set, *Comp. Mater. Sci.* 6 (1996) 15–50.
- G. Kresse, J. Furthmüller, Efficient iterative schemes for ab initio total-energy calculations using a plane-wave basis set, *Phys. Rev. B* 54 (1996) 11169–11186.
- J.P. Perdew, K. Burke, M. Ernzerhof, Generalized gradient approximation made simple, *Phys. Rev. Lett.* 77 (1996) 3865–3868.
- G. Kresse, D. Joubert, From ultrasoft pseudopotentials to the projector augmented-wave method, *Phys. Rev. B* 59 (1999) 1758–1775.
- P.E. Blöchl, Projector augmented-wave method, *Phys. Rev. B* 50 (1994) 17953–17979.
- J.K. Nørskov, J. Rossmeisl, A. Logadottir, L. Lindqvist, J.R. Kitchin, T. Bligaard, H. Jónsson, Origin of the overpotential for oxygen reduction at a fuel-cell cathode, *J. Phys. Chem. B* 108 (2004) 17886–17892.
- Ö. Bekaroglu, Synthesis of phthalocyanines and related compounds, *J. Porphyr. Phthalocyanines* 4 (2000) 465–473.
- M. Lu, M. Zhang, C.-G. Liu, J. Liu, L.-J. Shang, M. Wang, J.-N. Chang, S.-L. Li, Y.-Q. Lan, Stable dioxin-linked metallophthalocyanine covalent organic frameworks (COFs) as photo-coupled electrocatalysts for CO_2 reduction, *Angew. Chem. Int. Ed.* 60 (2021) 4864–4871.
- Z. Meng, J. Luo, W. Li, K.A. Mirica, Hierarchical tuning of the performance of electrochemical carbon dioxide reduction using conductive two-dimensional metallophthalocyanine based metal-organic frameworks, *J. Am. Chem. Soc.* 142 (2020) 21656–21669.
- M.-D. Zhang, D.-H. Si, J.-D. Yi, Q. Yin, Y.-B. Huang, R. Cao, Conductive phthalocyanine-based metal-organic framework as a highly efficient electrocatalyst for carbon dioxide reduction reaction, *Sci. China Chem.* 64 (2021) 1332–1339.
- Y. Chen, W. Cao, C. Wang, D. Qi, K. Wang, J. Jiang, Four dibutylamino substituents are better than eight in modulating the electronic structure and third-order

- nonlinear-optical properties of phthalocyanines, *Inorg. Chem.* 55 (2016) 3151–3160.
- [41] K. Chen, M. Cao, Y. Lin, J. Fu, H. Liao, Y. Zhou, H. Li, X. Qiu, J. Hu, X. Zheng, M. Shakouri, Q. Xiao, Y. Hu, J. Li, J. Liu, E. Cortés, M. Liu, Ligand engineering in nickel phthalocyanine to boost the electrocatalytic reduction of CO₂, *Adv. Funct. Mater.* (2021), <https://doi.org/10.1002/adfm.202111322>.
- [42] Y. Peng, L. Cui, S. Yang, J. Fu, L. Zheng, Y. Liao, K. Li, X. Zuo, D. Xia, Probing the influence of the conjugated structure and halogen atoms of poly-iron-phthalocyanine on the oxygen reduction reaction by x-ray absorption spectroscopy and density functional theory, *Electrochim. Acta* 154 (2015) 102–109.
- [43] K. Chen, H. Li, Y. Xu, K. Liu, H. Li, X. Xu, X. Qiu, M. Liu, Untying thioether bond structures enabled by "voltage-scissors" for stable room temperature sodium-sulfur batteries, *Nanoscale* 11 (2019) 5967–5973.
- [44] S. Chen, T. Luo, K. Chen, Y. Lin, J. Fu, K. Liu, C. Cai, Q. Wang, H. Li, X. Li, J. Hu, H. Li, M. Zhu, M. Liu, Chemical identification of catalytically active sites on oxygen-doped carbon nanosheet to decipher the high activity for electro-synthesis hydrogen peroxide, *Angew. Chem. Int. Ed.* 60 (2021) 16607–16614.
- [45] S. Khene, K. Lobb, T. Nyokong, Characterization of nickel tetrahydroxy phthalocyanine complexes and the electrocatalytic oxidation of 4-chlorophenol: correlation of theory with experiments, *Inorg. Chim. Acta* 362 (2009) 5055–5063.
- [46] K.C. Schultz, L. Supekova, Y. Ryu, J. Xie, R. Perera, P.G. Schultz, A genetically encoded infrared probe, *J. Am. Chem. Soc.* 128 (2006) 13984–13985.
- [47] H. Liao, T. Luo, P. Tan, K. Chen, L. Lu, Y. Liu, M. Liu, J. Pan, Unveiling role of sulfate ion in nickel-iron (oxy)hydroxide with enhanced oxygen-evolving performance, *Adv. Funct. Mater.* 31 (2021), 2102772.
- [48] H. Liao, P. Tan, R. Dong, M. Jiang, X. Hu, L. Lu, Y. Wang, H. Liu, Y. Liu, J. Pan, Insight into the amorphous nickel-iron (oxy)hydroxide catalyst for efficient oxygen evolution reaction, *J. Colloid Interface Sci.* 591 (2021) 307–313.
- [49] Y. Lin, K. Liu, K. Chen, Y. Xu, H. Li, J. Hu, Y.-R. Lu, T.-S. Chan, X. Qiu, J. Fu, M. Liu, Tuning charge distribution of FeN₄ via external N for enhanced oxygen reduction reaction, *ACS Catal.* 11 (2021) 6304–6315.
- [50] J. Fu, L. Zhu, K. Jiang, K. Liu, Z. Wang, X. Qiu, H. Li, J. Hu, H. Pan, Y.-R. Lu, T.-S. Chan, M. Liu, Activation of CO₂ on graphitic carbon nitride supported single-atom cobalt sites, *Chem. Eng. J.* 415 (2021), 128982.
- [51] S. Ren, D. Joulié, D. Salvatore, K. Torbensen, M. Wang, M. Robert, C. P. Berlinguette, Molecular electrocatalysts can mediate fast, selective CO₂ reduction in a flow cell, *Science* 365 (2019) 367–369.
- [52] Q. Wang, K. Liu, J. Fu, C. Cai, H. Li, Y. Long, S. Chen, B. Liu, H. Li, W. Li, X. Qiu, N. Zhang, J. Hu, H. Pan, M. Liu, Atomically dispersed s-block magnesium sites for electroreduction of CO₂ to CO, *Angew. Chem. Int. Ed.* 60 (2021) 25241–25245.
- [53] M. Liu, M. Liu, X. Wang, S.M. Kozlov, Z. Cao, P. De Luna, H. Li, X. Qiu, K. Liu, J. Hu, C. Jia, P. Wang, H. Zhou, J. He, M. Zhong, X. Lan, Y. Zhou, Z. Wang, J. Li, A. Seifitokaldani, D. Cao Thang, H. Liang, C. Zou, D. Zhang, Y. Yang, T.-S. Chan, Y. Han, L. Cavallo, T.-K. Sham, B.-J. Hwang, E.H. Sargent, Quantum-dot-derived catalysts for CO₂ reduction reaction, *Joule* 3 (2019) 1703–1718.
- [54] M. Zhang, W. Wei, S. Zhou, D.-D. Ma, A. Cao, X.-T. Wu, Q.-L. Zhu, Engineering a conductive network of atomically thin bismuthene with rich defects enables CO₂ reduction to formate with industry-compatible current densities and stability, *Energy Environ. Sci.* 14 (2021) 4998–5008.
- [55] K. Chen, K. Liu, P. An, H. Li, Y. Lin, J. Hu, C. Jia, J. Fu, H. Li, H. Liu, Iron phthalocyanine with coordination induced electronic localization to boost oxygen reduction reaction, *Nat. Commun.* 11 (2020) 4173.